Chemical Science

ROYAL SOCIETY OF CHEMISTRY

EDGE ARTICLE

View Article Online
View Journal

Check for updates

Cite this: DOI: 10.1039/d6sc00492j

All publication charges for this article have been paid for by the Royal Society of Chemistry

Non-ideal stoichiometry and thermochemistry of aqueous iridium oxide nanoparticles in proton-coupled electron transfer and oxygen-atom transfer

Justin L. Lee, †[ab] Saeed Saeed †[a] and James M. Mayer *[a]

Reported here are reactions of aqueous colloidal IrO_x nanoparticles (NPs) with proton-coupled electron transfer (PCET) and oxygen-atom transfer (OAT) organic reagents, determining the reaction stoichiometries and thermochemistry. IrO_x NPs have attracted much attention for their high electrocatalytic activity, but understanding of their fundamental reaction chemistry is limited. This IrO_x NP model system is simple, with UV-vis titrations demonstrating reversible interconversion between predominantly Ir^{IV} and predominantly Ir^{III} NPs. This simplicity allows studies that reveal their complex non-idealities. The NP redox chemistry has a "super-Nernstian" stoichiometry of $\sim 1.3H^+$ per $1e^-$ transferred during both PCET and OAT reactions, as measured with electrochemistry and chemical methods. Spectroelectrochemistry revealed a broad distribution of surface IrO_x–H bond dissociation free energies (BDFEs), becoming weaker as more H is added. Such variation in binding strengths—a non-ideal binding isotherm—is common for surface adsorbates. For IrO_x, the variation of BDFE(IrO–H)s is fit well to a Frumkin isotherm with a width of 6.5 kcal mol^{-1}. For OAT from the reactive oxygen atoms of IrO_x NPs, bracketing experiments gave 93 ± 24 kcal mol^{-1} for the average BDFE(O_xIr–O), with a predicted spread much larger than that for the BDFE(IrO–H). Taken together, the results show the importance of non-ideal stoichiometry and thermochemistry for IrO_x NPs, and they open a path to more complete models to understand catalytic redox reactions at such surfaces.

Received 17th January 2026
Accepted 2nd April 2026

DOI: 10.1039/d6sc00492j

rsc.li/chemical-science

1. Introduction

Redox reactions at metal-oxide/aqueous interfaces are essential to energy conversion, wastewater treatment, catalysis, corrosion, geochemistry, *etc.* These processes involve multiple steps on complex surfaces, and understanding them at atomistic detail is challenging. While much has been learned from experimental and computational studies of ideal surfaces, most surfaces have defects, irregularities, amorphous regions, and varying M:O:H stoichiometries.[1–5] In addition, electrochemical studies have often implicated $>1:1H^+/e^-$ stoichiometries, termed 'super-Nernstian' behaviour, as discussed below.[6–9]

Because of the complexity of oxide/water interfaces, direct experimental measurements of surface reactions are needed. Our approach is to study individual reaction steps on high surface area materials, especially colloidal nanoparticles (NPs).[10–14] While such measurements are an average over the diverse NP surfaces, or perhaps for that reason, some organizing principles are beginning to emerge.

Examined here are redox reactions of aqueous colloidal iridium oxide (IrO_x) nanoparticles (NPs).[15] IrO_x materials have long been known to undergo facile proton-coupled electron transfer (PCET)/hydrogen atom transfer (HAT) reactions. We have also recently reported oxygen atom transfer (OAT) reactions from these IrO_x NPs to molecular substrates.[14] These are some of the most fundamental reaction steps for redox-active oxides, and OAT is a rare example of a multi-electron process at a NP. Scheme 1 shows OAT with an O vacancy ($V_O^{\bullet\bullet}$), but lattice

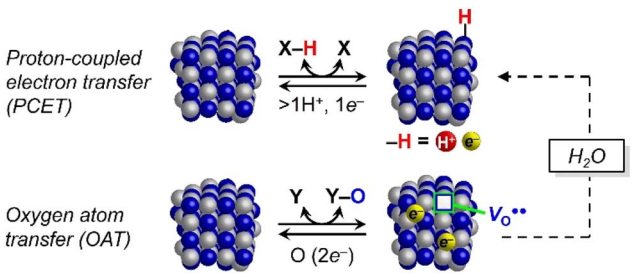

Scheme 1 Proton-coupled electron transfer and oxygen atom transfer of metal oxide NPs.

[a]Department of Chemistry, Yale University, New Haven, Connecticut 06520-8107, USA. E-mail: james.mayer@yale.edu

[b]Department of Chemistry, College of the Holy Cross, Worcester, MA 01610, USA

† These authors contributed equally to this work.

and adsorbed oxygen species can be difficult to distinguish for hydrous oxides (see below).[16]

A central parameter for surface reactions is the free energy of adsorption of the various intermediates. According to the Sabatier principle, a core intuition in heterogeneous catalysis, substrates and products should not bind too strongly or too weakly.[17,18] We have advocated that surface binding energies be quantified similarly to molecular bond strengths, as bond dissociation free energies (BDFEs) (eqn (1)).[19] Such BDFEs are central to molecular HAT and OAT reactions.[20–23] The heterogeneous catalysis/surface science literature uses the similar ΔG°_E parameter that is defined *vs.* H_2 or O_2 and is in the opposite direction (eqn (2) and (3), E = H or O).[16,17,24,25] ΔG°_H is often used as the 'descriptor' for multistep catalytic reactions, for instance in 'volcano plots' for the electrochemical hydrogen evolution reaction (HER).[26–29]

$$[\text{surface}] - E \rightarrow [\text{surface}] + E \quad \Delta G^\circ = \text{BDFE}([\text{Surf}] - E) \qquad (1)$$

$$\frac{1}{2}E_2 + [\text{surface}] \rightarrow [\text{surface}] - E \quad \Delta G^\circ_H \text{or } \Delta G^\circ_O \qquad (2)$$

$$\text{BDFE}([\text{Surf}] - E) = -\Delta G^\circ_E + \frac{1}{2}\text{BDFE}\left(E_{2(g)} \rightarrow 2E_{(\text{solution})}\right) \qquad (3)$$

Surface BDFEs and the Sabatier principle are, however, challenging to use for real surfaces. Even for flat, single crystal surfaces, surface – *E* BDFEs vary with surface coverage (θ_E), typically decreasing at higher θ.[1,2,24,30–32] Complex surfaces have various types of surface sites, with different BDFEs. Surfaces thus typically deviate from 'ideal' behaviour, with adsorption not well described by the ideal Langmuir isotherm.[5] Understanding non-idealities is particularly important for IrO_x and related oxides[33,34] because their amorphous, hydrous, or semi-crystalline forms can have higher OER activity than single-crystal surfaces.[35–37]

This study uses chemical and electrochemical methods to determine the stoichiometries and thermochemistry of redox reactions of IrO_x NPs. Studies were limited to Ir^{III}–Ir^{IV} interconversions to enable reversibility (avoiding catalysis). This report starts with various aspects of PCET reactions, then moves to OAT, and discusses possible links between these reactions.

2. Results

2.1 Synthesis & characterization of IrO_x NPs

The IrO_x NPs used in this study were prepared following a procedure from Mallouk *et al.*,[15] by first solvolysis of K_2IrCl_6 in basic water, followed by nitric acid-facilitated hydrolysis (SI Section S2, Fig. S1). The resulting dark purple colloidal solutions were 1.68 ± 0.01 mM [Ir] (by ICP-MS, see SI Section S2 and Fig. S3) and were used without further purification. Characterization of these NPs was reported in our recent OAT study.[14] The studies here were performed at pH 1.86 unless otherwise specified (pH adjusted with aqueous HNO_3 or NaOH, or by dilution with 18 MΩ H_2O). The IrO_x NPs were diluted 2-fold with 18 MΩ H_2O in UV-vis spectroscopic and pH titration experiments ([Ir] = 0.84 ± 0.01 mM), while other experiments used the as-prepared colloids. The optical feature at λ_{max} = 568 nm (top trace in Fig. 1A) is a useful spectroscopic handle for quantitative studies.

TEM images showed the NPs to be approximately spherical in shape, with an average diameter of 1.7 ± 0.2 nm (Fig. S1 and S2A). This corresponds to ~73 Ir atoms per average NP, most of which are estimated to be on the surface (~63 Ir, ~86%, SI Section S2). The large surface-to-core atom ratio is valuable for reactivity and catalytic studies. For simplicity, the as-prepared NPs are called IrO_x here, even though they likely have hydrous surfaces and an IrO_xH_y composition.

2.2 PCET reactivity for $Ir^{4+/3+}O_x(H^+)_m$ NPs

IrO_2 is known to access higher oxidation state, catalytically active surface species by PCET.[38–42] Murray and Mallouk[15,30] have shown the PCET behaviour of aqueous IrO_x NPs by cyclic voltammetry (CV) and rotated disk voltammetry. This section describes thermal PCET reactions of IrO_x NPs, their redox stoichiometry and reversibility, CVs as a function of pH, and finally the e^--to-H^+ stoichiometry.

2.2.1 Reduction of as-prepared IrO_x. Addition of 1,4-hydroquinone (H_2Q) to the aqueous IrO_x NPs caused an almost

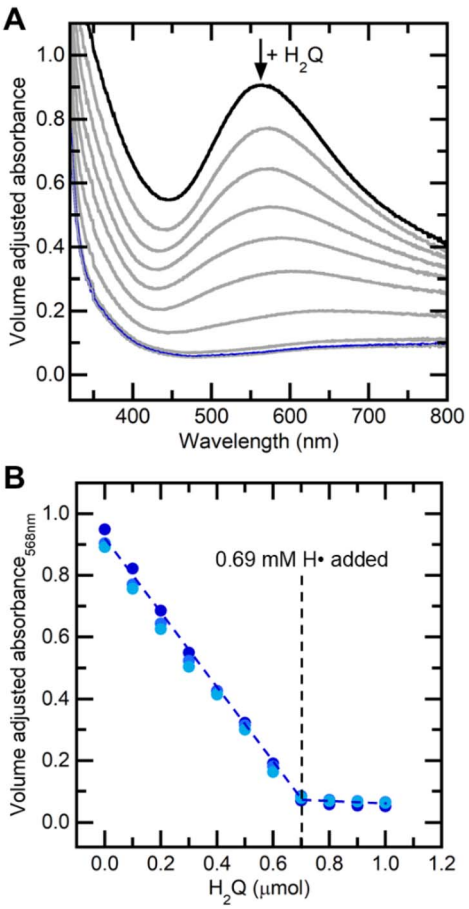

Fig. 1 (A) Spectra from a UV-vis titration of IrO_x + H_2Q. (B) Beer's law plot of corrected A_{568} *vs.* μmol of H_2Q added.

instantaneous bleach of the purple colour. Using small aliquots of H_2Q and monitoring spectrophotometrically, the IrO_x λ_{max} = 568 nm feature decreased incrementally until an almost featureless spectrum was reached (black to blue traces in Fig. 1). The absorbance plotted in Fig. 1B (A_{568}) was corrected for the increasing volume of the solution during titrations, and the optical baseline was adjusted to remove the small light scattering of the fully reduced NPs. The titration endpoint showed that 0.70 ± 0.01 μmol of H_2Q was required (from triplicate measurements). The linearity of the decrease in A_{568} showed that the IrO_x NPs obeyed the Beer–Lambert law, with ε_{568nm} = 1200 ± 40 M^{-1} cm^{-1} based on [Ir] = 0.84 mM.

A similar titration monitored by ^1H NMR spectroscopy showed the same endpoint. With increasing H_2Q added, NMR spectra showed its conversion to 1,4-benzoquinone (Q; Fig. S5). The [Q] increased linearly until the endpoint, and H_2Q was only observed past the endpoint, when there was no further formation of Q. Just as in the UV-vis experiment, the initial dark purple colour was bleached at the NMR endpoint (by eye).

H_2Q is a $2e^-$, $2H^+$ PCET reagent, equally well described as a donor of two hydrogen atoms. The 0.70 ± 0.01 μmol H_2Q endpoint thus has 1.40 μmol of reducing equivalents. The UV-vis titrations started with 1.68 μmol of Ir (2 mL of the 2-fold diluted 1.68 ± 0.01 mM as-prepared colloids), so the titration endpoint corresponds to 0.8 reducing equivalents per iridium. This ~80% reactivity is consistently observed with various PCET, ET, and OAT reagents (*vide infra*).

Based on these observations and the NP oxidation reactions described below, we assign the Ir oxidation state of the as-prepared NPs to be $Ir^{(3.8+)}$. IrO_x materials are often found in such non-integer average oxidation states, likely with a delocalized electronic structure, as IrO_2 is metallic.[43] The colourless reduced form at the end of the titration is assigned as essentially all Ir^{III}, as anticipated from the coordination chemistry of iridium and lack of low-energy LMCT or MLCT transitions.[44,45] The 568 nm absorbance has been suggested to be due to an Ir/Ir intervalence charge transfer, for instance on the basis of TD-DFT calculations.[46–48] The slight red-shift of the spectrum as the NPs are reduced is perhaps due to the shifts of their reduction potentials and/or to their slight growth, as suggested by the TEM images discussed below.

TEM images after reduction by H_2Q showed IrO_x NPs with a diameter of 1.8 ± 0.2 nm (Fig. S2B). This is within error of the as-prepared NPs, perhaps with a slight expansion. A slight elongation of the Ir–O bonds would be expected upon reduction due to the increase in the ionic radius. For instance, a 0.05 Å increase in the Ir–O bond length was reported for an electrodeposited IrO_2 film upon reduction.[49]

Analogous spectrophotometric redox titrations of the IrO_x NPs were performed with ascorbic acid and sodium ascorbate ($AscH_2$ and $AscH^-$), with the same spectral changes as in Fig. 1A. The same spectra were also obtained in titrations with $[Co^{II}(bpy)_3]^{2+}$, generally considered to be a mild, $1e^-$, outer-sphere reductant (Fig. S7).[50]

The endpoints of the $AscH_2$ and Asc^- titrations were the same as those with H_2Q (Fig. S8 and S9), as expected because these are all overall $2e^-$ reductants. With the Co^{II} solution, the endpoint was at twice the number of moles of reagent, within our experimental uncertainty. This is consistent with the reported $1e^-$ nature of this reductant.[50] The redox titrations with these reagents thus agree and well define the redox changes of the IrO_x NPs, specifically the number of electrons being added or removed. Discussion of the proton stoichiometries of these reactions, specifically how many H^+ are taken up by the IrO_x NPs upon reduction, is deferred to Section 2.2.3 below.

Scheme 2 Redox chemistry of IrO_x NPs.

2.2.2 Reversible redox reactivity of IrO_x NPs. Oxidation of IrO_x NPs was accomplished with sodium iodate ($NaIO_3$) and with oxone (containing peroxymonosulfate, $KHSO_5$). Other OAT reactions of the IrO_x NPs are described in Section 2.4.2 below. We tried but were unable to find an appropriate strong outer-sphere or PCET oxidant that was stable in these acid solutions and would not chemically change the IrO_x NPs (*e.g.*, Ce^{4+} could bind to the surface).

Oxone oxidized the as-prepared IrO_x NPs, as indicated by a darkening of the purple suspensions. Titration of the as-prepared NPs with Na_2SO_4 caused little change in the optical spectra (Fig. S11), implicating $KHSO_5$ as the reactive material. Scheme 2 shows images of the suspensions at different iridium oxidation levels. While quantitative titrations were not possible due to the instability of the particles with excess oxone (Fig. S12), the results are consistent with eqn (4) (which does not indicate the O and H stoichiometries).

$$Ir^{+3.8}O_x \text{ (as-prepared)} + SO_5^{2-} \rightarrow Ir^{+4}O_x + SO_4^{2-} \quad (4)$$

Sodium iodate readily oxidized the colourless H_2Q-reduced IrO_x NPs but appeared unreactive with the as-prepared NPs. Consistent with this limited reactivity, IO_3^- oxidized the H_2Q-reduced IrO_x NPs only to an absorbance close to that of as-prepared NPs. Iodate is primarily in its IO_3^- form at pH 1.86, based on its pK_a of 0.8.[51] Chemically reduced NPs (generated by treatment with 0.60 μmol H_2Q [1.2 μmol reducing equivalents]) were re-oxidized by 0.24 μmol IO_3^-, consistent with the $5e^-$ redox chemistry in eqn (5) (see below). The reduction of periodate stops at I_2 because the $Ir^{3.8}O_x$ NPs are not strong enough reductants to form I^- or I_3^-. This was confirmed by the oxidation of I^- by as-prepared NPs (see below).

$$IO_3^- + 5e^- + 6H^+ \rightarrow \tfrac{1}{2}I_2 + 3H_2O \quad (5)$$

The IrO_x NPs can undergo multiple reduction–oxidation cycles with H_2Q and IO_3^- (Fig. 2). This is consistent with the reversibility of the $Ir^{4+/3+}$ couple electrochemically (see ref. 30 and 15 and the next section). After a few cycles, a distinct feature at $\lambda_{max} = 454$ nm appeared that is characteristic of I_2,[52,53] consistent with eqn (5). The optical titrations and the cycling in Fig. 2A also show a slightly shifted λ_{max} for the IO^{3-}-oxidized NPs, from the original 568 nm to 575 nm. The magnitude of the absorbance remained relatively constant over the four cycles shown in Fig. 2B, while the bleach upon addition of H_2Q was less complete in later cycles. These changes could be due to the underlying I_2 absorbance and/or to small changes in the NPs upon repeated redox cycling.

2.2.3 The H^+/e^- ratio for PCET reactions of IrO_x NPs. The pH dependence of the electrochemical properties of IrO_x NPs and thin films has been examined in several prior studies. Some forms show shifts of 59 mV per pH unit, termed Nernstian behaviour, and interpreted as a 1 : 1 proton-to-electron stoichiometry.[54] However, hydrous forms of IrO_x (and many other redox-active oxides[6,55] typically have >59 mV pH^{-1} slopes (see the next section)).[30,56–58] Such super-Nernstian slopes have typically been interpreted as $>1:1H^+/e^-$ ratios, but not always.[59,60] To directly measure the stoichiometry for the NPs examined here, we applied our pH-monitoring approach previously developed for colloidal Au and TiO_2 NPs.[11,13]

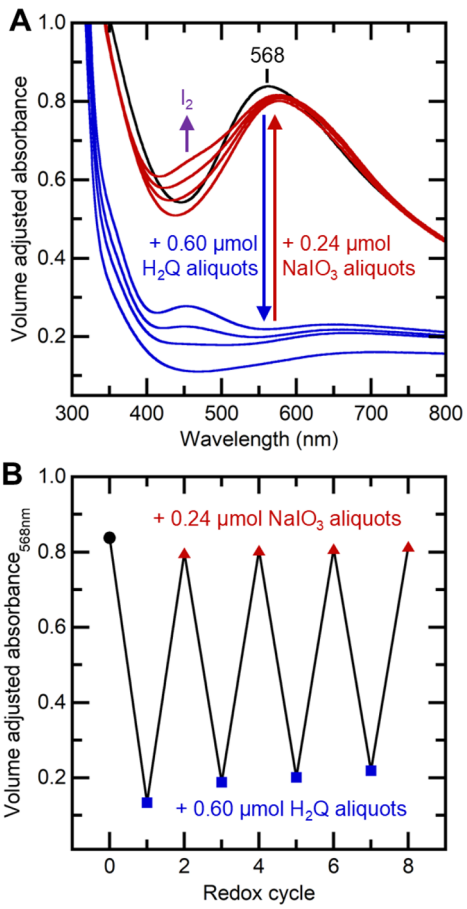

Fig. 2 Redox cycling of IrO_x NPs with H_2Q as the reductant and $NaIO_3$ as the oxidant. (A) UV-vis spectra after cycles of reduction (blue arrow and spectra) and oxidation (red arrow and spectra). (B) Volume-adjusted absorbances after successive cycles of reduction (blue) and then oxidation (red).

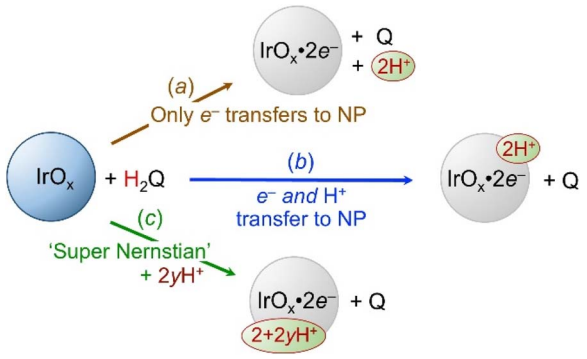

Scheme 3 Possible H^+ stoichiometries for IrO_x + H_2Q.

The $>1:1H^+/e^-$ stoichiometry of our IrO_x NP redox reactions was measured by chemical titrations with concurrent pH measurements, using $[H^+] = 10^{-pH}$. If titrations with H_2Q added only electrons to the IrO_x NPs, one H^+ would be released from H_2Q per e^- (Scheme 3(a), brown top reaction). Alternatively, if H_2Q transferred $H^\bullet$ ($e^- + H^+$) to IrO_x, there would be no change in $[H^+]$ (blue reaction, (b)). 'Super-Nernstian' behaviour, uptake of greater than $1H^+$ per e^-, would be indicated by a decrease in $[H^+]$ (green reaction, (c)).

For these experiments, the colloid was initially adjusted with $NaOH_{(aq)}$ to pH 2.90–3.10 ($[H^+]_{bulk}$ = 0.79–1.26 mM), so that changes of ±0.1 μmol in the amount of H^+ in the bulk solution could be detected with sufficient accuracy. An aliquot of H_2Q was added to this solution; after a few minutes, both the pH and UV-vis spectra were measured, and the cycle was repeated. The spectra (Fig. S6) showed the titration endpoint. The experiment

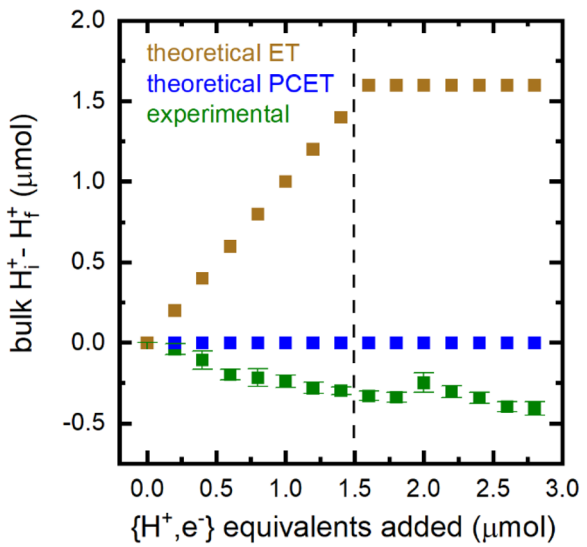

Fig. 3 Change in bulk H^+ (μmol) upon the addition of H^+, e^- (μmol; $\frac{1}{2}$ μmol H_2Q) calculated from the pH change. Brown represents the theoretical change for an ET, blue represents the change for PCET, and green represents the experimental results. Experimental data were corrected for dilution effects. The dashed line indicates the optical titration endpoint.

was performed with three separate solutions to ensure reproducibility.

Experimentally, addition of H_2Q to these IrO_x NPs resulted in an increase in pH, *i.e.*, a decrease in the amount of H^+ in solution. This is shown by the green squares in Fig. 3. After the optical titration endpoint, there was little change in the pH with additional H_2Q. The data showed that, for each reducing equivalent transferred from H_2Q to the NPs, the IrO_x took up $1.28H^+$. In addition to the one H^+ per e^- from H_2Q, IrO_x absorbed 0.28 additional H^+, in other words, super-Nernstian behaviour (eqn (6)).

$$IrO_x + \tfrac{1}{2}H_2Q + 0.28H^+ \rightarrow [IrO_x \cdot 1e^-, 1.28H^+] + \tfrac{1}{2}Q \qquad (6)$$

Experiments with the other reductants used above were consistent with the $1.3:1H^+:e^-$ ratio but the complex speciation of those reagents and their products prevented quantitative analysis of the observed pH changes (see Section S4, Fig. S10). The $1.3:1H^+:e^-$ results agree with the pH electrochemical results from Murray and from our laboratory (see the next section). These results are clearly different from the pure ET and $1:1e^-,H^+$ PCET pathways in Scheme 3 (see Section 3.1 below). The "extra" protons in the H_2Q and other reactions are provided by the pH 1.86 solution, which results from the nitric acid addition in one step of the synthesis.

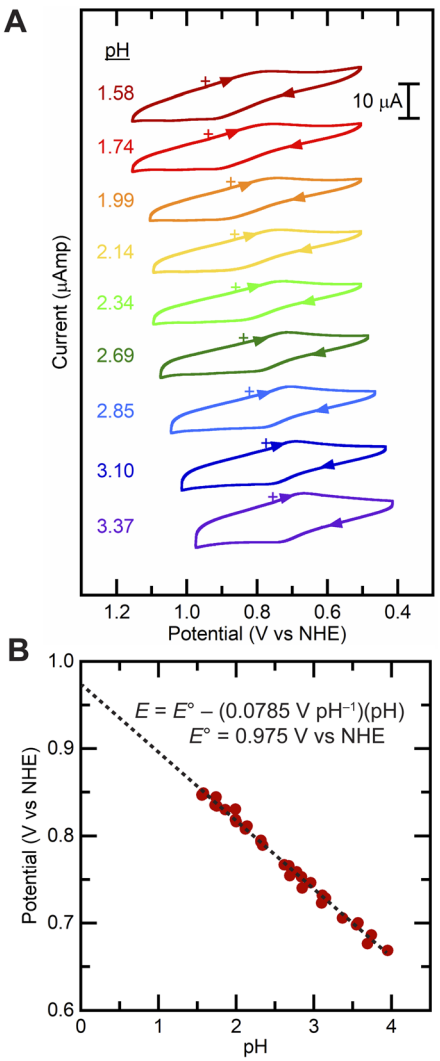

Fig. 4 (A) CVs of aqueous IrO_x NPs from pH 1.58–3.37; the + indicates the open circuit potential. (B) Pourbaix plot of $E_{\frac{1}{2}}$ values *vs.* pH for the $Ir^{IV/III}$ redox couple.

2.2.4 Electrochemical properties of IrO_x NPs. In agreement with prior studies,[15,30,40,41,61] our CVs of these colloidal IrO_x NPs showed two somewhat indistinct features; we focus here on the lower potential $Ir^{IV/III}$ couple (Fig. 4A and S4). The broadness of the waves is typical for CVs of colloidal NPs and is due to the non-ideal nature of their thermochemistry (described in the next section). The mid-point potential ($E_{\frac{1}{2}}$) of 0.83 V *vs.* NHE at pH 1.86 is consistent with the result below that as-prepared NPs oxidize I^- to I_2 or I_3^- ($E° = +0.621$ V or 0.536 V, respectively).[62]

The $E_{\frac{1}{2}}$ values from the CVs shifted with pH from 1.5–4 by 78.5 mV per pH unit (Fig. 4B). This slope was in excellent agreement with the 75 mV per pH reported by Murray *et al.* for phosphate-buffered IrO_x NPs in the pH 1–6 range.[30] The close agreement of Murray's and our slopes indicates that this deviation is not a measurement error from the broad waves. These results implicate a PCET process, consistent with the chemical titrations reported above.

The observed $E_{\frac{1}{2}}$ *vs.* pH slopes are ~30% larger than the 59.2 mV pH^{-1} expected for $1:1H^+:e^-$ transfers at 298 K. Such 'super-Nernstian' slopes, >59.2 mV pH^{-1}, are common for hydrous metal oxides and typically interpreted as a $>1H^+$ per e^- stoichiometry. From this perspective, the measured slope of 78.5 mV pH^{-1} translates into $1.33H^+/e^-$ (eqn (7)). This is in excellent agreement with the proton stoichiometry experiments described in the last section, which gave $1.28H^+/e^-$. This agreement is strong confirmation of the proton stoichiometry explanation for the super-Nernstian slope. This result is placed in a broader context in the Discussion below.

$$Ir^{IV}\,[\text{in } IrO_x] + e^- + 1.3H^+ \rightleftharpoons Ir^{III}\,[\text{in } IrO_x](H^+)_{1.3} \qquad (7)$$

2.3 PCET thermochemistry of $[IrO_x]$–H

2.3.1 Thermochemistry in a super-Nernstian system. A standard $1e^-/1H^+$ PCET reaction is characterized by a free energy $\Delta G°_{PCET}$, a $1e^- + 1H^+$ reduction potential $E°$, and an X–H BDFE, since $1e^- + 1H^+ \equiv H^\bullet$ (eqn (8)). The $\Delta G°_{PCET}$ and −BDFE are simply related by the constant C_G, which is 52.8 kcal mol^{-1} in water (eqn (9), for $E°$ *vs.* NHE at pH 0, or for $E°$ *vs.* RHE at any a_{H^+}).[19]

For $1H^+/1e^-$ reactions:

$$X + e^- + H^+ \rightarrow X\text{–}H \quad X + H^\bullet \rightarrow X\text{–}H \qquad (8)$$

$$\Delta G°_{PCET} = -FE°(1H^+/1e^-) = -BDFE(X-H) - C_G \qquad (9)$$

The IrO_x NP system, however, transfers 1.3 protons per electron, based on the electrochemical and pH studies in the last two sections. [Such behaviour has been termed super-Nernstian (see reviews[6]) and has been previously reported for hydrous IrO_x and generally.] The non-1 : 1 stoichiometry means that the $\Delta G°$ for reaction (7) is not simply a BDFE. What follows are our initial ideas; we have not found any related thermochemical analyses of

super-Nernstian reactions in the literature. We expect to return to this topic in a future publication.

For a super-Nernstian reaction that transfers $1 + s$ protons per electron, the free energy ΔG_{10} can be represented as a BDFE plus s times the proton chemical potential $\mu_{H^+} = -2.303RT \times$ pH (eqn (10)).

For $(1 + s)H^+/1e^-$ reactions:

$$\underbrace{X - H_{1+s} \rightarrow X + H^{\bullet}}_{\Delta G_{10}=\mathrm{BDFE(X-H)}} \underbrace{+sH^+}_{+s\mu_{H^+}} \quad (10)$$

For the IrO_x NP system discussed here, the $s\mu_{H^+}$ term is quite small. With $s = 0.3$ and pH = 1.83, $s\mu_{H^+} = 0.8$ kcal mol^{-1} (35 meV). Thus, the ΔG_{10} and BDFE for IrO_x–H are numerically close, roughly within the uncertainties of the analysis. To further illustrate that this is a small effect, we return to the E/pH dashed line in Fig. 3B above, with a 78.5 mV pH^{-1} slope and a y intercept ($E°$) of 0.975 V *vs.* NHE. Requiring a fixed 1 : 1 PCET slope of 0.059 V pH^{-1} moves the intercept only 1.7 kcal mol^{-1} (74 meV) lower at most (Fig. S14). We also emphasize that all the thermochemical studies in this report were carried out at pH 1.86, so that the $s\mu_{H^+}$ term is constant and does not affect relative energies. Based on this analysis, the thermodynamic discussion that follows will ignore the $1.33H^+/e^-$ stoichiometry and use the normal BDFE parameter.

2.3.2 A non-ideal isotherm for H-binding to IrO_x NPs. The measured aqueous PCET $E_{\frac{1}{2}}$ values extrapolated to pH 0 ($\cong E°$) give the surface BDFE(IrO_x–H) at the standard state. We use 50% coverage (θ_H) as our standard state, where $\theta_H = 1 - \theta_H = 0.5$. $\theta_H = 0$ corresponds to the fully oxidized $Ir^{4+}O_x$, and $\theta_H = 1$ indicates the fully reduced Ir^{3+} NPs. A system is "ideal" when the values of E vary with θ_H according to the Langmuir isotherm (eqn (11)). There is a very close analogy between eqn (11) and the Nernst equation for a solution potential, where the [Red] relates to θ_H and $[O_x] \equiv 1 - \theta_H$ (eqn (17) below). The $\theta_H = 0.5$ standard state for eqn (11) is directly analogous to the [Red] = $[O_x]$ standard state for the Nernst equation.

$$E_{\mathrm{Langmuir}} = E°_{\theta=0.5} - 0.059 \log\left(\frac{\theta_H}{1-\theta_H}\right) \quad (11)$$

To experimentally measure the binding isotherm for hydrogen on IrO_x NPs, we adapted a spectroelectrochemical approach previously developed for nickel oxide electrodes.[32] Briefly, an IrO_x NP colloid was poised at a specific electrochemical potential by controlled potential electrolysis, and after equilibration the UV-vis spectrum was recorded (Fig. 5B). These measurements were conducted at various E_{app} from 0.53 to 1.13 V *vs.* NHE at pH 1.86; as indicated by dashed and coloured vertical lines in Fig. 5A. Applying more anodic potentials resulted in oxidation beyond $Ir^{4.0+}$. Further details are discussed in Section S5.

The 568 nm absorbance decreased at more cathodic E_{app}, where the NPs were more reduced, and increased at anodic E_{app} (Fig. 5B). These changes were fully reversible. Waiting for equilibration and the reversibility of the absorbance show that these experiments measure thermodynamic properties. As established above, the A_{568nm} directly gives [Ir^{IV}] or, equivalently, the average oxidation state n of Ir (Ir^{n+}) (eqn (12)). This is readily converted to the fraction of Ir ions that are formally Ir^{IV}, $f(Ir^{IV})$, and to the coverage of H (eqn (13) and (14)).

$$A_{568} = \varepsilon_{568}[Ir^{IV}] \quad (12)$$

$$f(Ir^{IV}) = \frac{A_{568}(E)}{A_{568}(100\%\ \mathrm{Ir(IV)})} \quad (13)$$

$$\theta_H = 1 - f(Ir^{IV}) = f(Ir^{III}) \quad (14)$$

The experimental isotherm, the dependence of θ_H on E_{app}, is shown as the coloured points in Fig. 5C. The measured

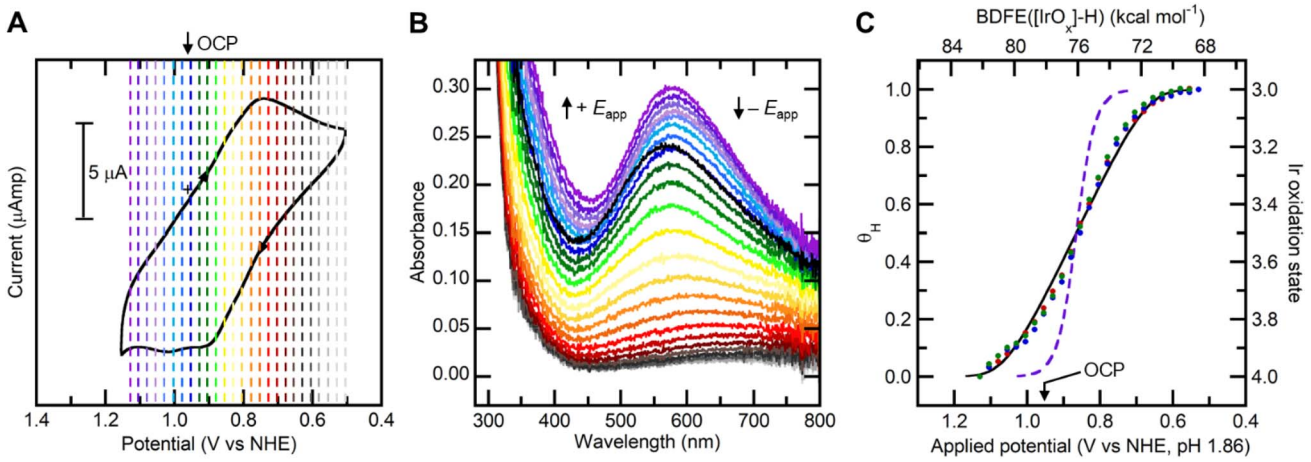

Fig. 5 (A) CV of IrO_x NPs. Coloured lines indicated applied potential steps at 0.025 V increments. (B) Optical spectra at different applied potentials. The colours of the absorbance spectra correspond to the colour of the applied potentials in Fig. 5A. (C) Plot of hydrogen coverage and Ir oxidation state as a function of applied potential and BDFE([IrO_x]–H). Coloured points indicate experimental data fitted to the Frumkin isotherm (black line; eqn (15)). The purple dashed line corresponds to the H-binding isotherm as described by the Langmuir isotherm (eqn (11)) and Nernst equation (eqn (17) below).

isotherm is quite broad, needing a change of 320 mV to move from 10% to 90% θ_H. The ideal Langmuir isotherm is much narrower, making this change over only 113 mV (the purple dashed line in Fig. 5C). The broadness of the isotherm is the primary origin of the broad CV waves in Fig. 4A.

The measurements fit well to a non-ideal Frumkin isotherm (black line, eqn (15)).[63,64] The century-old Frumkin isotherm simply adds a term linear in θ_H to the Langmuir isotherm (eqn (11)). The conclusion that surface binding is non-ideal is consistent with the discussion above about real surfaces, especially small nanoparticles.[5]

$$E_{\text{Frumkin}} = E_{\theta=0.5} - (0.0592\ \text{V})\log\left(\frac{\theta_H}{1-\theta_H}\right) + C(\theta_H - 0.5) \quad (15)$$

As a check, the midpoint of the fit (0.87 V) is within 40 mV of the $E_{1/2}$ measured by CV of the colloid at pH 1.86, as it should be. In addition, the isotherm in Fig. 5C is consistent with the as-prepared IrO_x NPs being mostly, but not completely, reduced by excess I^- (Fig. S13). The $E°(I_2/I^-)$ of ~0.62 V lies close to the bottom end of the isotherm, and the effective potential was higher due to the excess of I^- over I_2. The isotherm also predicts $\theta_H = 0.2$ and $Ir^{3.8+}$ for the as-prepared NPs, from their open circuit potential (OCP) value (Fig. 5C), in agreement with the titrations above. All the results are consistent with this Frumkin isotherm.

Fitting the data to the Frumkin equation gave $C = 0.28$ V, with free energy $FC = 0.28$ eV (6.5 kcal mol^{-1}). In some presentations, C is replaced by the unitless parameter $g = FC/RT$ (=11 in this case).[65,66] Given the width of the isotherm, the BDFE([IrO_x]–H) should be considered to have a range from 73 to 79 kcal mol^{-1}, with a midpoint of 76 kcal mol^{-1}.

2.4 OAT reactivity of IrO_x NPs

We recently reported that IrO_x NPs can oxidize substrates by oxygen atom transfer, including phosphines to phosphine oxides and a thioether to its sulfoxide (and slowly to the sulfone).[14] Here we extend those studies and compare them with the PCET chemistry described above.

2.4.1 Comparison of IrO_x reduction by OAT and PCET reagents. The reduction of IrO_x NPs by the water-soluble phosphine bis(*p*-sulfonatophenyl)phenylphosphine dianion (PAr_3) is remarkably similar to the reduction by H_2Q. The UV-vis titrations of IrO_x with PAr_3 and H_2Q showed almost identical spectra and endpoints: 0.66 ± 0.02 μmol for PAr_3 *vs.* 0.69 ± 0.01 μmol for H_2Q (Fig. S17).[14] This further supports the $Ir^{3.8+}$ oxidation state in the as-prepared NPs.

While PAr_3 and H_2Q are both 2e$^-$ reductants, phosphines accept O atoms while H_2Q typically donates H atoms. ^{18}O studies showed that OAT from IrO_x to PAr_3 forms some sort of vacant site, which is rapidly filled by a water molecule.[14] The process of O-removal and H_2O addition apparently forms the same product as the reduction by H_2Q.[14,67] To confirm this, we repeated the proton stoichiometry titration using PAr_3 instead of H_2Q. The pH and [H^+] change with PAr_3 (Fig. S18) were essentially identical to those for H_2Q (Fig. 3).

Overall, the similarities between the PAr_3 and H_2Q reactions reaffirm the implicit assumption above that these reactions are all under thermodynamic control. These are two quite different reagents, but they add the same number of reducing equivalents and form the same IrO_xH_y NP product.

2.4.2 Thermochemistry and barriers for IrO_x OAT reactions. The H_2Q-reduced IrO_x NPs are oxidized by iodate (IO_3^-) and oxone (SO_5^{2-}),[14] as mentioned above, and also by periodate (IO_4^-) (Fig. S19) and chlorine bleach (NaOCl/Cl_2) (Fig. S20). IO_3^- oxidizes the NPs roughly to the level of the as prepared material, $Ir^{3.8+}$, but the other reagents take the NPs to the all-Ir^{IV} state (Scheme 2 above) and perhaps beyond.

In the other direction, the as-prepared NPs are reduced by PAr_3 and methionine (Fig. S21–S25),[14] and also by excess nitrite ($NaNO_2$, Fig. S26). Nitrate formation was demonstrated by ^{15}N NMR ($^{15}NO_3^-$ from $^{15}NO_2^-$, Fig. S27). However, titration with nitrite did not show a sharp endpoint and nitrite is a complicated reagent that can disproportionate in acid solutions.

Many of these net OAT reactions are listed in order of decreasing estimated Y–O BDFEs in Scheme 4 (mostly converted from BDEs: see SI Section S7). As expected, the reagents with high affinities to accept an O atom reduce the IrO_x NPs (arrows

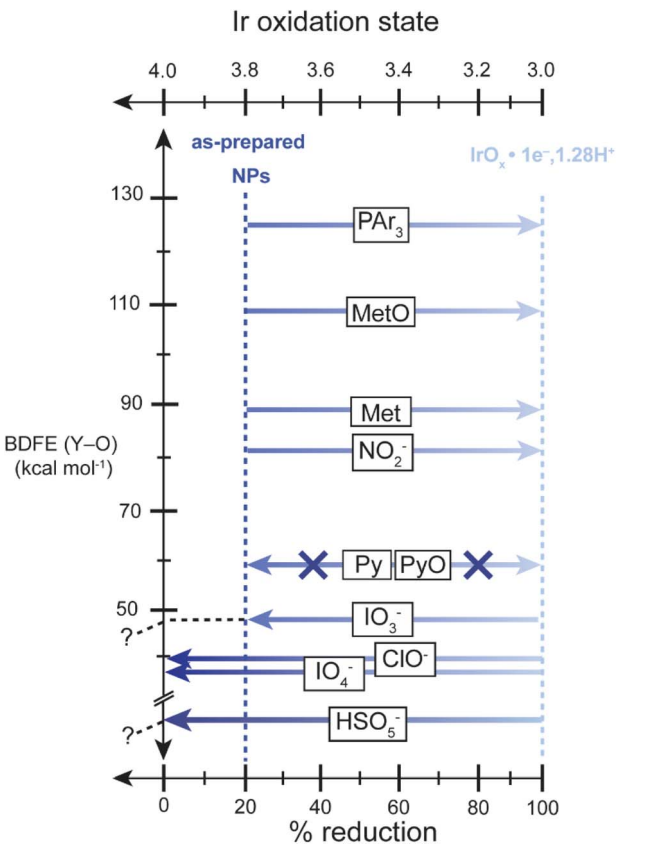

Scheme 4 Summary of IrO_x net OAT reactions: reagents that reduce the NPs (forward arrows) *vs.* oxidize the NPs (reverse arrows), listed by estimated BDFE(Y–O). See SI Section S7 for BDFE references and analysis. No reactions were observed with pyridine or pyridine *N*-oxide. The horizontal blue arrows are shaded to mimic the light colour of the reduced NPs (at right) *vs.* the dark purple of the oxidized NPs (at left). BDFE values for IO_3^- and HSO_5^- were not found, so these arrows are labelled with "?".

pointing to the right), and those that have weak Y–O bonds are good O-atom donors and oxidize the NPs (arrows to the left).

These reagents cover a huge range of driving forces for the OAT reactions, at least 87 kcal mol^{-1}. This range of ΔG corresponds to a change in K_{eq} of $\geq 10^{64}$. The results in Scheme 4 provide some insights into the OAT thermochemistry of the IrO_x NPs, as discussed below.

In contrast, no reaction was observed between the IrO_x NPs and pyridine derivatives. The as-prepared IrO_x NPs were not reduced by pyridine (py) or 4-CN-pyridine, and the H_2Q-reduced NPs were not oxidized by pyridine-*N*-oxide (pyO, Fig. S29–S31). The lack of reaction with both py and pyO indicates a kinetic barrier for OAT. In contrast, the HAT/PCET reactions of these IrO_x NPs all seem to follow their thermochemistry without substantial kinetic limitation.

3. Discussion

3.1 IrO_x NPs: a simple model system that reveals complexities

From one perspective, this colloidal IrO_x NP system is simple. Chemical reactions reversibly cycle the NPs between predominantly Ir^{IV} and predominantly Ir^{III} (for the 80% of the Ir that is redox active). The reaction stoichiometry sets the redox level of the product NPs, so the same thermodynamic product is formed regardless of the reagent. The same product is formed in PCET, HAT, and OAT reactions that give the same average Ir^{n+}. This reversibility and generality have enabled understanding of the intrinsic underlying complexity of the IrO_x NPs.

Based on our titrations and measurements of total Ir by ICP-MS, 80% of the Ir ions in these NPs are redox active. Gambarella, Murray, *et al.* reported the same result for IrO_x NPs at pH 1.4, using coulometry (though almost all the Ir was electroactive at higher pH values).[30] We previously estimated that the ~1.7 nm IrO_x NP diameter corresponds to 4–5 unit cells across and roughly 86% of the Ir ions are on the surface.[14] While there are uncertainties in both the percent electroactive and the percent at the surface, the values are consistent with the redox reactions and H addition primarily involving surface sites. This is consistent with the lack of a change in size by TEM.[14] However, oxides in water often have a hydrous, partly amorphous shell, which muddies the definition of a surface atom.

All the chemical reactions studied here, PCET, HAT, and OAT, have the same 1.3 : 1 proton-to-electron stoichiometry, or H^+ per redox equivalent. The $H^+ : e^-$ ratio is important because it determines how the reduction potential varies with pH. This follows from the Nernst or Langmuir equations, with $[XH_m{}^{(m-n)+}]/[X] \equiv (\theta/1-\theta)$ (eqn (16)–(21)). Examples with integer $H^+ : e^-$ ratios are widely recognized, in Pourbaix's comprehensive Atlas and elsewhere.[68,69] E/pH slopes that are not integer multiples of 59 mV pH^{-1} (m/n) have also long been known and are typically interpreted as a non-integer $H^+ : e^-$ stoichiometry. However, other effects could lead to such super-Nernstian slopes. For example, recent papers by Suntivich and co-workers assumed 1 : $1H^+ : e^-$ ratios and attributed super-Nernstian slopes to changes in E°.[7,34,70] For our IrO_x NPs, the non-integer stoichiometry was established by a direct chemical method, the change in pH upon reaction (Fig. 3), in addition to electrochemistry. The 1.3 : 1 ratio must be the thermodynamic preference of the IrO_x, although the origin of this preference is not known. For these NPs, we take full H coverage, $\theta_H = 1$, to be $1.3H^+$ for every Ir^{III}.

$$\text{For: } X + mH^+ + ne^- \rightarrow XH_m{}^{(m-n)+} \tag{16}$$

$$E_{Nernst} = E^\circ - \frac{RT}{nF}\ln\left\{\frac{[XH_m{}^{(m-n)+}]}{[X][H^+]^m}\right\} \tag{17}$$

$$E_{Langmuir} = E^\circ_{\theta=0.5} - 0.059\log\left(\frac{\theta_H}{(1-\theta_H)[H^+]^{m/n}}\right) \tag{18}$$

$$= E^\circ_{\theta=0.5} - (0.0592\text{ mV})\left\{\frac{m}{n}pH - \log\left(\frac{\theta_H}{(1-\theta_H)}\right)\right\} \tag{19}$$

The IrO_x NPs studied here have non-ideal H adsorption in terms of both stoichiometry and thermochemistry. The adsorption energies follow a Frumkin isotherm rather than a Langmuir isotherm. θ_H as a function of pH and $E_{applied}$ does not follow eqn (18) and (19). We have not found literature that addresses this case of both non-integer stoichiometry and a non-ideal binding isotherm, and we are not prepared to do this fully here. Still, the model system studies reported here show large non-idealities that are not captured by current models.

To simplify the thermochemical discussions that follow, the remainder of this Discussion will assume a $1 : 1H^+ : e^-$ stoichiometry. As explained above, this assumption has little numerical effect on the parameters because the pH was kept constant at 1.83 that is close to the standard state of pH 0.

3.2 H-atom binding energies

3.2.1 Fitting to a Frumkin isotherm. The large surface area, high concentration, and optical absorbance of the IrO_x NPs enable the determination of the H-binding isotherm by spectroelectrochemistry (Section 2.3). It was established that the system reached equilibrium at each point (each applied potential or amount of reagent).

The measured Frumkin isotherm is about 3 times broader than ideal Langmuir behaviour, with a long linear middle portion. The ratio of Ir^{III} to Ir^{IV} in the NPs changes much more slowly with potential than in ideal behaviour. The non-ideality of these IrO_x NPs contradicts the common assumption that surface concentrations are good proxies for surface activities, and the common assumption of a single free energy of adsorption. The measured isotherm implies a range of IrO_x–H BDFEs, from 73–79 kcal mol^{-1}.

The non-ideality of the binding energies is not surprising, as discussed in the next section.[5] To quote and expand Gileadi's colourful analogy:[66]

"Solid surfaces are rarely homogeneous. There are active sites on which the standard free energy of adsorption is high, and there are less-active sites…. This is much like people entering a movie theater with unmarked seats: the best seats are

taken first, and the worst remain for late-comers. Some like to sit together while others prefer to leave empty seats".[66]

3.2.2 Generality of the Frumkin isotherm. Frumkin isotherms have been used to describe electrochemical and chemical surface binding for a century.[71] Hydrogen adsorption on metal surfaces has long been known to become weaker with increasingly coverage.[72] The non-ideality is of roughly the same magnitude for H_2 gas adding to metals and for electrosorption of H^+ onto a Pt(111) crystal face.[73] Frumkin C parameters of 0.2–0.3 V have been measured for the first oxidations of hydrous, partially disordered IrO_2 and Co/phosphate films,[33,74] for highly ordered RuO_2(110) films,[70] for calcined NiO films in contact with various buffers and solvents,[24] and for oleylamine-capped WO_3 nanorods in THF,[31,32,75] in addition to the aqueous colloidal IrO_x NPs studied here. Yet colloidal, oleate-capped CeO_{2-x} NPs in THF have a much broader isotherm,[26] and the 2nd oxidation of the RuO_2(110) films was almost ideal (C close to 0).[70] Theory has provided insights into the differences between the two RuO_2(110) redox couples (assuming $1:1H^+:e^-$).[34]

The generality of the Frumkin isotherm is perhaps surprising. It seems to apply equally well to the highly ordered RuO_2(110) films, to hydrous, partly amorphous IrO_2 and Co/phosphate films, and the IrO_x NPs studied here. The 1.7 nm IrO_x NPs are only a few unit cells across, and a high fraction of surface sites are edges, corners, and defects, if they are faceted at all. Not-so-different results have been obtained with oxides, various single crystal metal surfaces,[72] and metal nanoparticles.[24] The Frumkin isotherm was developed based on inter-adsorbate interactions, but these observations suggest a generality that transcends any single cause.

The Frumkin isotherm is the first-order approximation to a Langmuir isotherm[66] and can be thought of as the first term of a Taylor series expansion in θ. Taking a_0 in eqn (20) as the Langmuir isotherm (eqn (18)), and x as a small perturbation from that function, the Frumkin linear $C\theta$ term is simply the a_1x term. From this perspective, any small effect that causes deviation from ideality should, to a first approximation, yield a Frumkin isotherm. The observation of a Frumkin isotherm does not provide insight into the origin of the non-ideality.

$$f(x) = a_0 + a_1x + a_2x^2 + a_3x^3 + \ldots \quad (20)$$

The breadth of the isotherm is likely due to a variety of factors. These include (some of these overlap): (i) a diversity of surface sites, especially due to the small size of the NPs, (ii) the range of NP sizes, (iii) other surface heterogeneities, for instance due to surface O/OH/OH_2 groups, (iv) inter-adsorbate repulsion (as in Frumkin's original derivation), (v) changes in the structure and bonding of the nanoparticles upon H addition, (vi) variability in the points of zero charge, both among different NPs and upon H addition, and (vii) the presence of surface dipoles. The very broad isotherm for H on CeO_2 nanoparticles was suggested to be due to increasing lattice strain as individual Ce^{4+} ions are reduced to localized and form much larger Ce^{3+} ions,[26] but this is not the case for IrO_x due to its metallic bonding and delocalized electrons.

Still, it is remarkable that the isotherm data follow a single, smooth curve. On an irregular surface such as a small NP, one might have expected a subset of the sites to have much higher or lower affinities for H, which would have led to a more irregular experimental isotherm. Instead, for most materials, the Frumkin $C(\theta - 0.5)$ seems to well describe an average over all the potential non-idealities.

3.3 Connecting H- and O-atom thermochemistry

OAT and HAT/PCET are two quite different classes of reactions, yet the products are related simply by a water molecule, as illustrated in Scheme 5.[67] This stoichiometric connection has long been recognized but is often not highlighted in discussion.[67] Both double H-atom addition and removal of an O-atom result in a $2e^-$ reduction. OAT formally gives a vacancy in the NP ($V_O^{\cdot\cdot}$), which in aqueous media is rapidly filled by H_2O. This forms the same $MO_x{\cdot}2H$ as HAT/PCET to the NP. This equivalence is evident for the IrO_x reactions with H_2Q and PAr_3 discussed above, in their identical titration endpoints and amounts of proton uptake.

The triangle scheme in Scheme 5 also serves as a thermochemical cycle between PCET and OAT reactivity. Because it is a closed loop, the sum of the three $\Delta G°$s around the cycle must be zero, as shown in eqn (21), moving counterclockwise from the oxidized form at the top. This equation allows the calculation of any free energy from the other two. While more work is needed to experimentally define the $\Delta G°$(OAT to Y) and $\Delta G°$(H_2O binding to $V_O^{\cdot\cdot}$), this connection between HAT and OAT provides valuable insights.

$$\Delta G^\circ(\text{OAT to Y}) + \Delta G^\circ(\text{H}_2\text{O binding to } V_O^{\cdot\cdot}) + 2\Delta G^\circ(\text{HAT to X}) = 0 \quad (21)$$

The $\Delta G°$ for H_2O dissociation (bottom of Scheme 5) is thus a key parameter in connecting HAT and OAT

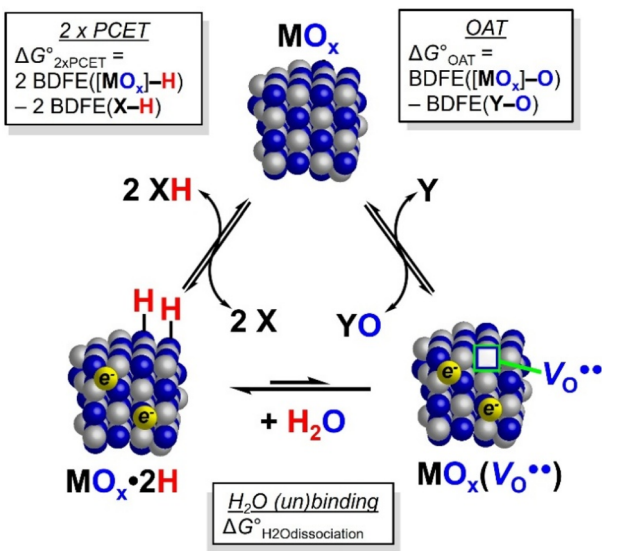

Scheme 5 Triangle scheme connecting HAT and OAT.

thermochemistry.[58] Unfortunately, we have found little information about H_2O binding energies in aqueous solutions when the O being lost is formally a lattice oxygen [the product of OAT] (SI Section S7). Calculations of H_2O binding energies for an ideal, oxidized, stoichiometric $(IrO_2)_{115}(H_2O)_{88}$ nanoparticle *in vacuo* gave $\Delta G^{\circ}_{H_2O\ diss}$ values from −26 to −36 kcal mol^{-1}.[76] The binding energy for H_2O to a bare RuO_2 surface was calculated to be −33 kcal mol^{-1}.[77]

Following this kind of analysis, the OAT thermochemistry of the IrO_x NPs is bracketed by the ladder of reactions in Scheme 4 above (see SI Section S7). This approach has long been used in molecular and solid-state chemistries. For instance, Soper *et al.* bracketed the BDE of a $V^{V}{\equiv}O$ bond in $[(^{Ph}isq)(^{Ph}ibq)V^{IV}(O)Cl]$ to be 73 ± 14 kcal mol^{-1} (ref. 78) by reacting its complex with seven OAT reagents with 60 < BDE[Y–O] < 133 kcal mol^{-1}.[21,79] The free energies for loss of O_2 from solid binary metal oxides as a function of temperature were summarized in an 'Ellingham diagram' 80 years ago.[80]

For IrO_x NPs, the driving force for the OAT reactions includes both the O_xIr–O BDFE and the ΔG° for H_2O binding. This H_2O binding is specifically to the oxygen vacancy resulting from Ir–O bond cleavage (Scheme 5). With this approach, the ladder of OAT reactions in Scheme 4 brackets the combination of the BDFE(O_xIr–O) and the $\Delta G^{\circ}_{H_2O\ binding}$ (eqn (22), in kcal mol^{-1}). Unfortunately, this analysis gives only a broad range because reagents with intermediate Y–O BDFEs, such as pyO, were kinetically unreactive. If $\Delta G^{\circ}_{H_2O\ binding}$ is taken to be −30 kcal mol^{-1}, BDFE(Ir–O) is estimated to be 93 ± 24 kcal mol^{-1} (eqn (23))

$$\sim 87(\mathrm{Met}) > \mathrm{BDFE}(O_xIr-O) - \Delta G^{\circ}_{H_2O\ binding} > \sim 40(IO_4^-) \text{With } \Delta G^{\circ}_{H_2O\ binding} \sim -30 \text{ kcal mol}^{-1}, \quad (22)$$

$$117 > \mathrm{BDFE}(O_xIr\text{–}O) > 70, \text{ or } \mathrm{BDFE}(O_xIr\text{–}O) = 93 \pm 24 \text{ kcal mol}^{-1} \quad (23)$$

Thermochemical cycles such as Scheme 5 can be used in multiple ways. For instance, Scheme 6 shows how the ΔG° for the pyridine *N*-oxide ($pyO_{(aq)}$) oxidation of fully reduced IrO_xH_n NPs (eqn (25)) can be determined without knowledge of the $\Delta G^{\circ}_{H_2O\ binding}$. The O removed from pyO is transferred to solution (eqn (24)) and then picks up two H from the reduced IrO_x NPs (eqn (25) and (26)) to form the product water. The ΔG° (eqn (27)) is estimated to be −13 kcal mol^{-1}. More details and references are given in SI Section S7, together with a related calculation for OAT to methionine.

$$pyO_{(aq)} \rightleftharpoons py_{(aq)} + O_{(aq)} \qquad BDFE(py\text{–}O) \quad (24)$$

$$IrO_x{\bullet}2H_{(NP)} \rightleftharpoons IrO_{x(NP)} + 2\,H{\bullet}_{(aq)} \qquad 2BDFE(IrO_x\text{–}H) \quad (25)$$

$$2H{\bullet}_{(aq)} + O_{(aq)} \rightleftharpoons H_2O_{(l)} \qquad -\Delta G^{\circ}_{H2O(l),atom} \quad (26)$$

$$IrO_x{\bullet}2H_{(NP)} + pyO_{(aq)} \rightleftharpoons IrO_{x(NP)} + py_{(aq)} + H_2O_{(l)} \quad (27)$$

$$\Delta G^{\circ}_{(25)} = 2BDFE(IrO_x\text{–}H) + BDFE(Y\text{–}O) - \Delta G^{\circ}_{H2O(l),atom}$$

Scheme 6 ΔG° for IrO_xH_n + pyO → IrO_x + py + H_2O.

Under the pH 1.83 reaction conditions, the product py of reaction (27) will be protonated, which will add more driving force. Yet this reaction does not proceed. The absence of reaction is therefore due to a kinetic barrier ($\Delta G^{\ddagger}$) and not due to the reaction being uphill. This contrasts with the HAT/PCET reactions above that seem to parallel the thermochemistry in all cases.

3.4 Non-ideality in O-atom thermochemistry

The next layer of the thermochemical analysis of O-atom transfer reactions is the likelihood of broad ranges of the OAT free energy parameters. Scheme 5 and eqn (21) show that OAT is related to twice the HAT energetics, so to a first approximation the spread of Ir–O BDFEs should be twice that of the IrO–H BDFEs, or *ca.* ∼13 kcal mol^{-1}. This follows from an O-atom being a 2e$^-$ oxidant *vs.* the 1e$^-$ reductant H$^{\bullet}$.

The range of H_2O binding energies noted above will also contribute to the non-ideality of O-atom binding. The calculations of the ideal $(IrO_2)_{115}(H_2O)_{88}$ NP mentioned above found eleven different Ir binding sites for water and that hydrogen-bonding networks were important.[76] The diversity of sites, H-bonding networks, and binding energies is likely even larger for our hydrous IrO_x NPs in aqueous solution. Perhaps most importantly, we have yet no information about which of the possible water dissociations form a vacancy that can accept an O atom.

A combined surface-science and DFT study examined 4-layer (9 Å) films of rutile $IrO_2(100)$ grown on an Ir(111) crystal surface.[81] The surface was "oxygen-rich", with roughly one O per Ir beyond the stoichiometric $IrO_2(100)$ surface, in the less-stable atop binding configuration. BDFE(Ir–O) for these extra O atoms was very small, decreasing from 23–18 kcal mol^{-1} with increasing O coverage. Considering all the surface Ir–O bonds, the calculations showed a 47 kcal mol^{-1} binding energy range.

These calculations show the remarkable diversity and complexity of IrO_2 single crystal and idealized NP surfaces. For our IrO_x NPs, the chemistry of Ir–O bonds will be more complex than that of IrO–H bonds.

4. Conclusions

The redox reactions of aqueous colloidal IrO_x NPs are non-ideal in both their stoichiometry and thermochemistry.

These 1.7 nm-diameter NPs in acidic water have been developed as a simple model system for interfacial reactivity at a redox-active metal oxide. Focusing only on the Ir^{IV}/Ir^{III} redox couple, various PCET/HAT ($e^- + H^+$) and oxygen-atom transfer (OAT) reactions are reversible, with ∼80% of the Ir ions electroactive. The colloids can be set at any average Ir redox level, and the same thermodynamic product is formed with each reagent.

The reactions of the IrO_x NPs all have the same 'super-Nernstian' stoichiometry, with 1.3 protons adding to the IrO_x surface with each electron added. The non-integer stoichiometry was demonstrated electrochemically and by directly measuring the H^+ taken up upon reduction. Non-integer PCET

is common for hydrous oxides,[30,56–58] but its origin is not well understood.

Spectroelectrochemical studies showed that changes in the $[Ir^{IV}]/[Ir^{III}]$ ratio in the NPs required much larger changes in applied potential than predicted by the Nernst equation. The data fit well to a non-ideal Frumkin isotherm. Approximating the reactions as H-atom transfers ($1H^+ : 1e^-$), the distribution of BDFE($[IrO_x]$–H) has a midpoint of 76 kcal mol^{-1} and a spread of 6.5 kcal mol^{-1} as a function of H saturation (θ_H). The isotherm for O-atom removal from the IrO_x NPs is estimated to be much wider than that for HAT, due in part to OAT being a formal $2e^-$ transfer.

The non-ideal stoichiometry and thermochemistry are core features of the redox chemistry of this 'simple' IrO_x NP model system and many others. Oxide–water interfaces should not be assumed to follow ideal Nernstian or Langmuirian behaviour (as is often done). The thermochemistry very nicely fits a simple two-parameter Frumkin isotherm, and the reason for the generality of this isotherm is discussed. The accuracy of the mathematically simple Frumkin isotherm provides quantitative understanding and provides a path forward to more realistic models. New models are needed because the non-ideality of (nano)materials is likely an advantage in many applications.

Author contributions

The conception of the project was by J. L. L. and J. M. M., and the experiments and analyses were performed by J. L. L. and S. S. J. M. M. was the research advisor, assisting with project goal selection, project focus, and experiment interpretation. All authors participated in manuscript preparation and editing, with final editing by J. M. M.

Conflicts of interest

There are no conflicts to declare.

Data availability

The datasets supporting this article have been uploaded as part of the supplementary information (SI). Supplementary information: reagents, NP synthesis, characterization of NPs, UV-vis and NMR spectra, thermochemical tables of Y–O substrates. See DOI: https://doi.org/10.1039/d6sc00492j.

Acknowledgements

This research made extensive use of Yale University's Chemical and Biophysical Instrumentation Center (CBIC; RRID:SCR_021738; equipment was purchased with funds from Yale University). We also thank the Yale Institute for Nanoscience and Quantum Engineering (YINQE) and Dr Sungwoo Sohn, as well as the Yale Analytical and Stable Isotope Center (YASIC) and Jonas Karosas. The work was funded predominantly by the U.S. Department of Energy, Office of Science, Basic Energy Sciences (award No. DE-SC0021298).

Notes and references

1 G. D. Halsey, The Role of Surface Heterogeneity in Adsorption, in *Advances in Catalysis*, Elsevier, 1952, vol. 4, pp 259–269, DOI: 10.1016/S0360-0564(08)60616-1.
2 M. Boudart, Kinetics on Ideal and Real Surfaces, *AIChE J.*, 1956, **2**(1), 62–64, DOI: 10.1002/aic.690020113.
3 G. E. Brown, V. E. Henrich, W. H. Casey, D. L. Clark, C. Eggleston, A. Felmy, D. W. Goodman, M. Grätzel, G. Maciel, M. I. McCarthy, K. H. Nealson, D. A. Sverjensky, M. F. Toney and J. M. Zachara, Metal Oxide Surfaces and Their Interactions with Aqueous Solutions and Microbial Organisms, *Chem. Rev.*, 1999, **99**(1), 77–174, DOI: 10.1021/cr980011z.
4 O. Q. Carvalho, P. Adiga, S. K. Murthy, J. L. Fulton, O. Y. Gutiérrez and K. A. Stoerzinger, Understanding the Role of Surface Heterogeneities in Electrosynthesis Reactions, *iScience*, 2020, **23**(12), 101814, DOI: 10.1016/j.isci.2020.101814.
5 J. M. Mayer, Site Heterogeneity and Broad Surface-Binding Isotherms in Modern Catalysis: Building Intuition beyond the Sabatier Principle, *J. Catal.*, 2024, **439**, 115725, DOI: 10.1016/j.jcat.2024.115725.
6 L. D. Burke and M. E. G. Lyons, Electrochemistry of Hydrous Oxide Films, in *Modern Aspects of Electrochemistry*, ed.R. E. White, J. O. Bockris and B. E. Conway, Springer US, Boston, MA, 1986, vol. 18, pp 169–248, DOI: 10.1007/978-1-4613-1791-3.
7 D.-Y. Kuo, J. K. Kawasaki, J. N. Nelson, J. Kloppenburg, G. Hautier, K. M. Shen, D. G. Schlom and J. Suntivich, Influence of Surface Adsorption on the Oxygen Evolution Reaction on IrO_2 (110), *J. Am. Chem. Soc.*, 2017, **139**(9), 3473–3479, DOI: 10.1021/jacs.6b11932.
8 C. Liang, Y. Katayama, Y. Tao, A. Morinaga, B. Moss, V. Celorrio, M. Ryan, I. E. L. Stephens, J. R. Durrant and R. R. Rao, Role of Electrolyte pH on Water Oxidation for Iridium Oxides, *J. Am. Chem. Soc.*, 2024, **146**(13), 8928–8938, DOI: 10.1021/jacs.3c12011.
9 N. P. Holzapfel, V. Augustyn and V. Balland, Fundamentals of Proton-Insertion Coupled Electron Transfer (PICET) in Metal Oxides for Aqueous Batteries, *ACS Energy Lett.*, 2025, **10**(3), 1143–1164, DOI: 10.1021/acsenergylett.4c03076.
10 C. N. Valdez, A. M. Schimpf, D. R. Gamelin and J. M. Mayer, Proton-Controlled Reduction of ZnO Nanocrystals: Effects of Molecular Reductants, Cations, and Thermodynamic Limitations, *J. Am. Chem. Soc.*, 2016, **138**(4), 1377–1385, DOI: 10.1021/jacs.5b12182.
11 J. L. Peper, N. E. Gentry, B. Boudy and J. M. Mayer, Aqueous TiO_2 Nanoparticles React by Proton-Coupled Electron Transfer, *Inorg. Chem.*, 2022, **61**(2), 767–777, DOI: 10.1021/acs.inorgchem.1c03125.
12 R. G. Agarwal and J. M. Mayer, Coverage-Dependent Rate-Driving Force Relationships: Hydrogen Transfer from Cerium Oxide Nanoparticle Colloids, *J. Am. Chem. Soc.*, 2022, **144**(45), 20699–20709, DOI: 10.1021/jacs.2c07988.

13 N. E. Gentry, A. Kurimoto, K. Cui, J. L. Cleron, C. M. Xiang, S. Hammes-Schiffer and J. M. Mayer, Hydrogen on Colloidal Gold Nanoparticles, *J. Am. Chem. Soc.*, 2024, **146**(21), 14505–14520, DOI: 10.1021/jacs.4c00507.

14 J. L. Lee, N. E. Gentry, J. L. Peper, S. Hetzel, C. Quist, F. S. Menges and J. M. Mayer, Oxygen Atom Transfer Reactions of Colloidal Metal Oxide Nanoparticles, *ACS Nano*, 2025, **19**(10), 10289–10300, DOI: 10.1021/acsnano.4c17955.

15 Y. Zhao, E. A. Hernandez-Pagan, N. M. Vargas-Barbosa, J. L. Dysart and T. E. Mallouk, A High Yield Synthesis of Ligand-Free Iridium Oxide Nanoparticles with High Electrocatalytic Activity, *J. Phys. Chem. Lett.*, 2011, **2**(5), 402–406, DOI: 10.1021/jz200051c.

16 J. K. Nørskov, T. Bligaard, A. Logadottir, S. Bahn, L. B. Hansen, M. Bollinger, H. Bengaard, B. Hammer, Z. Sljivancanin, M. Mavrikakis, Y. Xu, S. Dahl and C. J. H. Jacobsen, Universality in Heterogeneous Catalysis, *J. Catal.*, 2002, **209**(2), 275–278, DOI: 10.1006/jcat.2002.3615.

17 A. J. Medford, A. Vojvodic, J. S. Hummelshøj, J. Voss, F. Abild-Pedersen, F. Studt, T. Bligaard, A. Nilsson and J. K. Nørskov, From the Sabatier Principle to a Predictive Theory of Transition-Metal Heterogeneous Catalysis, *J. Catal.*, 2015, **328**, 36–42, DOI: 10.1016/j.jcat.2014.12.033.

18 H. Ooka, J. Huang and K. S. Exner, The Sabatier Principle in Electrocatalysis: Basics, Limitations, and Extensions, *Front. Energy Res.*, 2021, **9**, 654460, DOI: 10.3389/fenrg.2021.654460.

19 R. G. Agarwal, S. C. Coste, B. D. Groff, A. M. Heuer, H. Noh, G. A. Parada, C. F. Wise, E. M. Nichols, J. J. Warren and J. M. Mayer, Free Energies of Proton-Coupled Electron Transfer Reagents and Their Applications, *Chem. Rev.*, 2022, **122**(1), 1–49, DOI: 10.1021/acs.chemrev.1c00521.

20 F. R. Mayo, Rate Constants in the Gas-Phase Oxidation of Alkanes and Alkyl Radicals, in *Advcances in Chemistry, Oxidation of organic compounds*, American Chemical Society, Washington, DC, 1968, vol. 2.

21 R. H. Holm, Metal-Centered Oxygen Atom Transfer Reactions, *Chem. Rev.*, 1987, **87**(6), 1401–1449.

22 J. M. Mayer, Understanding Hydrogen Atom Transfer: From Bond Strengths to Marcus Theory, *Acc. Chem. Res.*, 2011, **44**(1), 36–46, DOI: 10.1021/ar100093z.

23 C. T. Campbell, Energies of Adsorbed Catalytic Intermediates on Transition Metal Surfaces: Calorimetric Measurements and Benchmarks for Theory, *Acc. Chem. Res.*, 2019, **52**(4), 984–993, DOI: 10.1021/acs.accounts.8b00579.

24 M. García-Diéguez, D. D. Hibbitts and E. Iglesia, Hydrogen Chemisorption Isotherms on Platinum Particles at Catalytic Temperatures: Langmuir and Two-Dimensional Gas Models Revisited, *J. Phys. Chem. C*, 2019, **123**(13), 8447–8462, DOI: 10.1021/acs.jpcc.8b10877.

25 Z. Paal and P. G. Menon, *Hydrogen Effects in Catalysis*, CRC Press, 2020, DOI: 10.1201/9781003065807.

26 B. E. Conway and J. O. Bockris, Electrolytic Hydrogen Evolution Kinetics and Its Relation to the Electronic and Adsorptive Properties of the Metal, *J. Chem. Phys.*, 1957, **26**(3), 532–541, DOI: 10.1063/1.1743339.

27 T. Bligaard, J. K. Nørskov, S. Dahl, J. Matthiesen, C. H. Christensen and J. Sehested, The Brønsted–Evans–Polanyi Relation and the Volcano Curve in Heterogeneous Catalysis, *J. Catal.*, 2004, **224**(1), 206–217, DOI: 10.1016/j.jcat.2004.02.034.

28 J. Zheng, W. Sheng, Z. Zhuang, B. Xu and Y. Yan, Universal Dependence of Hydrogen Oxidation and Evolution Reaction Activity of Platinum-Group Metals on pH and Hydrogen Binding Energy, *Sci. Adv.*, 2016, **2**(3), e1501602, DOI: 10.1126/sciadv.1501602.

29 N. Dubouis and A. Grimaud, The Hydrogen Evolution Reaction: From Material to Interfacial Descriptors, *Chem. Sci.*, 2019, **10**(40), 9165–9181, DOI: 10.1039/C9SC03831K.

30 A. A. Gambardella, N. S. Bjorge, V. K. Alspaugh and R. W. Murray, Voltammetry of Diffusing 2 Nm Iridium Oxide Nanoparticles, *J. Phys. Chem. C*, 2011, **115**(44), 21659–21665, DOI: 10.1021/jp206987z.

31 R. G. Agarwal, H. J. Kim and J. M. Mayer, Nanoparticle O-H Bond Dissociation Free Energies from Equilibrium Measurements of Cerium Oxide Colloids, *J. Am. Chem. Soc.*, 2021, **143**(7), 2896–2907, DOI: 10.1021/jacs.0c12799.

32 H. Noh and J. M. Mayer, Medium-Independent Hydrogen Atom Binding Isotherms of Nickel Oxide Electrodes, *Chem*, 2022, **8**(12), 3324–3345, DOI: 10.1016/j.chempr.2022.08.018.

33 C. Liang, R. R. Rao, K. L. Svane, J. H. L. Hadden, B. Moss, S. B. Scott, M. Sachs, J. Murawski, A. M. Frandsen, D. J. Riley, M. P. Ryan, J. Rossmeisl, J. R. Durrant and I. E. L. Stephens, Unravelling the Effects of Active Site Density and Energetics on the Water Oxidation Activity of Iridium Oxides, *Nat. Catal.*, 2024, **7**(7), 763–775, DOI: 10.1038/s41929-024-01168-7.

34 L. Zhang, J. Kloppenburg, C.-Y. Lin, L. Mitrovic, S. Gelin, I. Dabo, D. G. Schlom, J. Suntivich and G. Hautier, Atomistic Understanding of Hydrogen Coverage on RuO_2 (110) Surface under Electrochemical Conditions from *Ab Initio* Statistical Thermodynamics, *J. Phys. Chem. C*, 2025, **129**(8), 4043–4051, DOI: 10.1021/acs.jpcc.4c07229.

35 T. Reier, D. Teschner, T. Lunkenbein, A. Bergmann, S. Selve, R. Kraehnert, R. Schlögl and P. Strasser, Electrocatalytic Oxygen Evolution on Iridium Oxide: Uncovering Catalyst-Substrate Interactions and Active Iridium Oxide Species, *J. Electrochem. Soc.*, 2014, **161**(9), F876–F882, DOI: 10.1149/2.0411409jes.

36 H. Yu, F. Liao, W. Zhu, K. Qin, J. Shi, M. Ma, Y. Li, M. Fang, J. Su, B. Song, L. Li, R. R. Zairov, Y. Ji, M. Shao and Q. Shao, Two-Dimensional Amorphous Iridium Oxide for Acidic Oxygen Evolution Reaction, *ChemCatChem*, 2023, **15**(19), e202300737, DOI: 10.1002/cctc.202300737.

37 R. V. Mom, L. J. Falling, O. Kasian, G. Algara-Siller, D. Teschner, R. H. Crabtree, A. Knop-Gericke, K. J. J. Mayrhofer, J.-J. Velasco-Vélez and T. E. Jones, Operando Structure–Activity–Stability Relationship of Iridium Oxides during the Oxygen Evolution Reaction, *ACS Catal.*, 2022, **12**(9), 5174–5184, DOI: 10.1021/acscatal.1c05951.

38 J. Gao, Y. Liu, B. Liu and K. W. Huang, Progress of Heterogeneous Iridium-Based Water Oxidation Catalysts, *ACS Nano*, 2022, **16**(11), 17761–17777, DOI: 10.1021/acsnano.2c08519.

39 R. Sharma, M. A. Karlsen, P. Morgen, J. Chamier, D. B. Ravnsbæk and S. M. Andersen, Crystalline Disorder, Surface Chemistry, and Their Effects on the Oxygen Evolution Reaction (OER) Activity of Mass-Produced Nanostructured Iridium Oxides, *ACS Appl. Energy Mater.*, 2021, **4**(3), 2552–2562, DOI: 10.1021/acsaem.0c03127.

40 C. Bozal-Ginesta, R. R. Rao, C. A. Mesa, X. Liu, S. A. J. Hillman, I. E. L. Stephens and J. R. Durrant, Redox-State Kinetics in Water-Oxidation IrOx Electrocatalysts Measured by Operando Spectroelectrochemistry, *ACS Catal.*, 2021, **11**(24), 15013–15025, DOI: 10.1021/acscatal.1c03290.

41 C. Bozal-Ginesta, R. R. Rao, C. A. Mesa, Y. Wang, Y. Zhao, G. Hu, D. Antón-García, I. E. L. Stephens, E. Reisner, G. W. Brudvig, D. Wang and J. R. Durrant, Spectroelectrochemistry of Water Oxidation Kinetics in Molecular versus Heterogeneous Oxide Iridium Electrocatalysts, *J. Am. Chem. Soc.*, 2022, **144**(19), 8454–8459, DOI: 10.1021/jacs.2c02006.

42 G. Kwon, S. H. Chang, J. E. Heo, K. J. Lee, J. K. Kim, B. G. Cho, T. Y. Koo, B. J. Kim, C. Kim, J. H. Lee, S. M. Bak, K. A. Beyer, H. Zhong, R. J. Koch, S. Hwang, L. M. Utschig, X. Huang, G. Hu, G. W. Brudvig, D. M. Tiede and J. Kim, Experimental Verification of Ir 5d Orbital States and Atomic Structures in Highly Active Amorphous Iridium Oxide Catalysts, *ACS Catal.*, 2021, **11**(15), 10084–10094, DOI: 10.1021/acscatal.1c00818.

43 J. M. Kahk, C. G. Poll, F. E. Oropeza, J. M. Ablett, D. Céolin, J.-P. Rueff, S. Agrestini, Y. Utsumi, K. D. Tsuei, Y. F. Liao, F. Borgatti, G. Panaccione, A. Regoutz, R. G. Egdell, B. J. Morgan, D. O. Scanlon and D. J. Payne, Understanding the Electronic Structure of IrO_2 Using Hard-X-Ray Photoelectron Spectroscopy and Density-Functional Theory, *Phys. Rev. Lett.*, 2014, **112**(11), 117601, DOI: 10.1103/PhysRevLett.112.117601.

44 L. J. Yellowlees and K. G. Macnamara, Iridium, in *Comprehensive Coordination Chemistry II*, 2003, vol. 6, pp. 147–246.

45 R. H. Crabtree, High Oxidation State Complexes of Rhodium and Iridium, in *Comprehensive Coordination Chemistry III*, 2021, pp. 159–170.

46 H. Ooka, Y. Wang, A. Yamaguchi, M. Hatakeyama, S. Nakamura, K. Hashimoto and R. Nakamura, Legitimate Intermediates of Oxygen Evolution on Iridium Oxide Revealed by in Situ Electrochemical Evanescent Wave Spectroscopy, *Phys. Chem. Chem. Phys.*, 2016, **18**(22), 15199–15204, DOI: 10.1039/C6CP02385A.

47 S. Gottesfeld, J. D. E. McIntyre, G. Beni and J. L. Shay, Electrochromism in Anodic Iridium Oxide Films, *Appl. Phys. Lett.*, 1978, **33**(2), 208–210, DOI: 10.1063/1.90277.

48 Z. Pavlovic, C. Ranjan, Q. Gao, M. Van Gastel and R. Schlögl, Probing the Structure of a Water-Oxidizing Anodic Iridium Oxide Catalyst Using Raman Spectroscopy, *ACS Catal.*, 2016, **6**(12), 8098–8105, DOI: 10.1021/acscatal.6b02343.

49 Y. Mo, I. C. Stefan, W. B. Cai, J. Dong, P. Carey and D. A. Scherson, In Situ Iridium LIII-Edge X-Ray Absorption and Surface Enhanced Raman Spectroscopy of Electrodeposited Iridium Oxide Films in Aqueous Electrolytes, *J. Phys. Chem. B*, 2002, **106**(14), 3681–3686, DOI: 10.1021/jp014452p.

50 Y. Sasaki, H. Kato and A. Kudo, $[Co(bpy)_3)]^{3+/2+}$ and $[Co(phen)_3]^{3+/2+}$ Electron Mediators for Overall Water Splitting under Sunlight Irradiation Using Z-Scheme Photocatalyst System, *J. Am. Chem. Soc.*, 2013, **135**(14), 5441–5449, DOI: 10.1021/ja400238r.

51 D. Dalzel Perrin, *Dissociation Constants of Inorganic Acids and Bases in Aqueous Solution*, Pergamon, New York, New York, 1982.

52 A. D. Awtrey and R. E. Connick, The Absorption Spectra of I_2, I_3^-, I^-, IO_3^-, $S_4O_6^=$ and $S_2O_3^=$. Heat of the Reaction $I_3^- = I_2 + I^-$, *J. Am. Chem. Soc.*, 1951, **73**(4), 1842–1843, DOI: 10.1021/ja01148a504.

53 T. Labasque, C. Chaumery, A. Aminot and G. Kergoat, Spectrophotometric Winkler Determination of Dissolved Oxygen: Re-Examination of Critical Factors and Reliability, *Mar. Chem.*, 2004, **88**(1–2), 53–60, DOI: 10.1016/j.marchem.2004.03.004.

54 M. F. Yuen, I. Lauks and W. C. Dautremont-Smith, pH Dependent Voltammetry of Iridium Oxide Films, *Solid State Ionics*, 1983, **11**(1), 19–29, DOI: 10.1016/0167-2738(83)90058-9.

55 S. Fleischmann, J. B. Mitchell, R. Wang, C. Zhan, D. E. Jiang, V. Presser and V. Augustyn, Pseudocapacitance: From Fundamental Understanding to High Power Energy Storage Materials, *Chem. Rev.*, 2020, **120**(14), 6738–6782, DOI: 10.1021/acs.chemrev.0c00170.

56 L. D. Burke and T. A. M. Twomey, Influence of Ph on the Redox Behaviour of Hydrous Nickel Oxide, *J. Electroanal. Chem. Interfacial Electrochem.*, 1982, **134**(2), 353–362, DOI: 10.1016/0022-0728(82)80013-2.

57 C. Bock and V. I. Birss, Anion and Water Involvement in Hydrous Ir Oxide Redox Reactions in Acidic Solutions, *J. Electroanal. Chem.*, 1999, **475**(1), 20–27, DOI: 10.1016/S0022-0728(99)00330-7.

58 K. A. Stoerzinger, R. R. Rao, X. R. Wang, W. T. Hong, C. M. Rouleau and Y. Shao-Horn, The Role of Ru Redox in pH-Dependent Oxygen Evolution on Rutile Ruthenium Dioxide Surfaces, *Chem*, 2017, **2**(5), 668–675, DOI: 10.1016/j.chempr.2017.04.001.

59 L. D. Burke and D. P. Whelan, A Voltammetric Investigation of the Charge Storage Reactions of Hydrous Iridium Oxide Layers, *J. Electroanal. Chem. Interfacial Electrochem.*, 1984, **162**(1–2), 121–141.

60 D.-Y. Kuo, J. K. Kawasaki, J. N. Nelson, J. Kloppenburg, G. Hautier, K. M. Shen, D. G. Schlom and J. Suntivich, Influence of Surface Adsorption on the Oxygen Evolution Reaction on IrO_2 (110), *J. Am. Chem. Soc.*, 2017, **139**(9), 3473–3479, DOI: 10.1021/jacs.6b11932.

61 M. A. Petit and V. Plichon, Anodic Electrodeposition of Iridium Oxide Films, *J. Electroanal. Chem.*, 1998, **444**(2), 247–252, DOI: 10.1016/S0022-0728(97)00570-6.
62 C. Vanleugenhaghe, G. Valensi, M. Pourbaix and M. Pourbaix, Iodine, in *Atlas of Electrochemical Equilibria in Aqueous Solutions*, NACE International, 1974, pp. 614–626.
63 E. Gileadi, Adsorption in Electrochemistry, in *Electrosorption*, Springer, 1967, pp. 1–18.
64 A. J. Bard and L. R. Faulkner, Double-Layer Structure and Adsorption, in *Electrochemical Methods: Fundamentals and Applications*, John Wiley & Sons, Inc., 2001, pp. 534–579.
65 P. Delahay, *Double Layer and Electrode Kinetics*, Interscience Publishers, 1965.
66 E. Gileadi, *Electrode Kinetics for Chemists, Chemical Engineers, and Materials Scientists*, John Wiley & Sons, 1996, pp. 262–266, The discussion here, and the quoted text, are from.
67 T. Norby, M. Widerøe, R. Glöckner and Y. Larring, Hydrogen in Oxides, *Dalton Trans.*, 2004, (19), 3012–3018, DOI: 10.1039/B403011G.
68 M. Pourbaix, *Atlas of Electrochemical Equilibria in Aqueous Solutions*, National Association of Corrosion Engineers, 1974.
69 B. D. McCarthy and J. L. Dempsey, Decoding Proton-Coupled Electron Transfer with Potential-pKa Diagrams, *Inorg. Chem.*, 2017, **56**(3), 1225–1231, DOI: 10.1021/acs.inorgchem.6b02325.
70 B. Hu, D.-Y. Kuo, H. Paik, D. G. Schlom and J. Suntivich, Enthalpy and Entropy of Oxygen Electroadsorption on RuO_2(110) in Alkaline Media, *J. Chem. Phys.*, 2020, **152**(9), 094704, DOI: 10.1063/1.5139049.
71 *Grokipedia v2.0.*, https://grokipedia.com/page/alexander_frumkin, accessed January 14, 2026.
72 K. Christmann, Interaction of Hydrogen with Solid Surfaces, *Surf. Sci. Rep.*, 1988, **9**(1–3), 1–163, DOI: 10.1016/0167-5729(88)90009-X.
73 R. Rizo, E. Sitta, E. Herrero, V. Climent and J. M. Feliu, Towards the Understanding of the Interfacial pH Scale at Pt(111) Electrodes, *Electrochim. Acta*, 2015, **162**, 138–145, DOI: 10.1016/j.electacta.2015.01.069.
74 B. Moss, K. L. Svane, D. Nieto-Castro, R. R. Rao, S. B. Scott, C. Tseng, M. Sachs, A. Pennathur, C. Liang, L. I. Oldham, E. Mazzolini, L. Jurado, G. Sankar, S. Parry, V. Celorrio, J. M. Dawlaty, J. Rossmeisl, J. R. Galán-Mascarós, I. E. L. Stephens and J. R. Durrant, Cooperative Effects Drive Water Oxidation Catalysis in Cobalt Electrocatalysts through the Destabilization of Intermediates, *J. Am. Chem. Soc.*, 2024, **146**(13), 8915–8927, DOI: 10.1021/jacs.3c11651.
75 N. J. Gibson, G. A. Parada, B. Q. Mercado and J. M. Mayer, Colloidal Hexagonal Tungsten Oxide Nanorods: Synthesis, Characterization, and Proton-Coupled Electron Transfer, *Inorg. Chem.*, 2026, **65**(4), 2659–2668, DOI: 10.1021/acs.inorgchem.5c06029.
76 D. González, M. Sodupe, L. Rodríguez-Santiago and X. Solans-Monfort, Surface Morphology Controls Water Dissociation on Hydrated IrO_2 nanoparticles, *Nanoscale*, 2021, **13**(34), 14480–14489, DOI: 10.1039/d1nr03592d.
77 R. Mu, D. C. Cantu, X. Lin, V. A. Glezakou, Z. Wang, I. Lyubinetsky, R. Rousseau and Z. Dohnálek, Dimerization Induced Deprotonation of Water on RuO_2(110), *J. Phys. Chem. Lett.*, 2014, **5**(19), 3445–3450, DOI: 10.1021/jz501810g.
78 A. G. Hill, M. C. Castillo, J. Bacsa, K. S. Otte and J. D. Soper, Redox-Active Ligands Permit Multielectron O2 Homolysis and O-Atom Transfer at Exceptionally High-Valent Vanadyl Complexes, *J. Am. Chem. Soc.*, 2025, **147**(16), 13356–13369, DOI: 10.1021/jacs.4c18305.
79 R. H. Holm and J. P. Donahue, A Thermodynamic Scale for Oxygen Atom Transfer Reactions, *Polyhedron*, 1993, **12**, 571–589.
80 H. J. T. Ellingham, Transactions and Communications, *J. Chem. Technol. Biotechnol.*, 1944, **63**(5), 125–160, DOI: 10.1002/jctb.5000630501.
81 R. Rai, T. Li, Z. Liang, M. Kim, A. Asthagiri and J. F. Weaver, Growth and Termination of a Rutile IrO_2(100) Layer on Ir(111), *Surf. Sci.*, 2016, **652**, 213–221, DOI: 10.1016/j.susc.2016.01.018.